



Carbon-supported bimetallic Pd–Fe catalysts for vapor-phase hydrodeoxygenation of guaiacol



Junming Sun^{a,1}, Ayman M. Karim^{a,*}, He Zhang^b, Libor Kovarik^a, Xiaohong Shari Li^a, Alyssa J. Hensley^b, Jean-Sabin McEwen^b, Yong Wang^{a,b,*}

^a Institute for Integrated Catalysis, Pacific Northwest National Laboratory, Richland, WA 99352, United States

^b The Gene & Linda Voiland School of Chemical Engineering and Bioengineering, Washington State University, Pullman, WA 99164, United States

ARTICLE INFO

Article history:

Received 10 December 2012

Revised 25 March 2013

Accepted 18 May 2013

Available online 6 July 2013

Keywords:

Pd–Fe

Hydrodeoxygenation

Bimetallic catalysis

Bio-oil upgrading

Alloy catalyst

EXAFS

Carbon support

ABSTRACT

Carbon-supported metal catalysts (Cu/C, Fe/C, Pd/C, Pt/C, PdFe/C, and Ru/C) were characterized and evaluated for vapor-phase hydrodeoxygenation (HDO) of guaiacol (GUA), aiming at the identification/elucidation of active catalysts for high-yield production of completely hydrodeoxygenated products (e.g., benzene). Phenol was found to be the major intermediate on all catalysts. Saturation of the aromatic ring is the major pathway over the precious metal catalysts, forming cyclohexanone and cyclohexanol, followed by ring opening to form gaseous products. Base metal catalysts exhibit lower activity than the precious metal catalysts, but selectively form benzene along with small amounts of toluene, trimethylbenzene (TMB), and cresol without forming ring-saturated or ring-opening products. Compared with Fe/C and Pd/C, PdFe/C catalysts exhibit a substantially enhanced activity while maintaining the high selectivity to HDO products without ring saturation or ring opening. The enhanced activity of PdFe/C is attributed to the modification of Fe nanoparticles by Pd as evidenced by STEM, EDS, EXAFS, TPR, and theoretical calculations.

© 2013 Elsevier Inc. All rights reserved.

1. Introduction

Fast pyrolysis is potentially an attractive approach for the direct thermo-chemical conversion of lignocellulosic biomass to bio-oils [1–3]. The lignin-derived phenolic compounds (phenols, guaiacols, syringoles) formed during the fast pyrolysis are highly reactive and can undergo secondary reactions during the condensation step to produce oligomers [4,5]. In addition, during bio-oil upgrading, phenolic compounds have been reported to cause fast catalyst deactivation [6,7]. Therefore, it is highly desirable to defunctionalize these phenolic compounds via hydrodeoxygenation (HDO) with minimum H₂ consumption.

Early work indicated that conventional hydrodesulfurization (HDS)/hydrodenitrogenation (HDN) catalysts exhibit promising activity in HDO of phenolic compounds such as phenol, anisole, and guaiacol [8–12]. However, these metal–sulfide catalysts suffer from deactivation in the presence of high water content and the continuous addition of sulfur is required in the reactant stream to maintain the catalysts in the sulfide form. This last factor in

particular can cause serious problems for the downstream processes [11,13,14]. Alternative hydrotreating catalysts have been sought for bio-oil upgrading [6,13,15–20]. Among these, extensive research activities have focused on precious metal catalysts at high H₂ pressures [8–12,16,20–34]. These studies showed the tendency to saturate the aromatic ring before removing the oxygen groups, resulting in a large and costly consumption of H₂.

To date, vapor-phase HDO of biomass fast pyrolysis products have been mostly limited to zeolites [35–41] which suffer from low activity and are highly susceptible to coke formation [7,37]. Only a limited number of studies have been reported using supported metal catalysts [6,15,18,19,42–46]. Zhao et al. compared a group of transition metal phosphides, commercial Pd/Al₂O₃, and CoMoS/Al₂O₃ in HDO of guaiacol [15]. Metal phosphides showed promising HDO activity with benzene, phenol, and anisole being the predominant products, but they suffered from fast deactivation. Pd/Al₂O₃ was more active than the metal phosphides and the commercial CoMoS/Al₂O₃, but it produced mainly catechol [15]. Recently, Gates' group compared Pt/Al₂O₃ and Pt/HY catalysts in the HDO of anisole and guaiacol. Their results showed that the transalkylation activity of the catalyst was significantly affected by the type of acidic site [18,19]. A later study by Zhu et al. further confirmed the effect of acidic sites on the transalkylation activity in the HDO of anisole [17]. A very recent report indicates that Fe/SiO₂ shows a higher hydrodeoxygenation activity without saturation of

* Corresponding authors. Address: Institute for Integrated Catalysis, Pacific Northwest National Laboratory, Richland, WA 99352, United States (Y. Wang).

E-mail addresses: ayman.karim@pnnl.gov (A.M. Karim), yong.wang@pnnl.gov (Y. Wang).

¹ Current address: The Gene & Linda Voiland School of Chemical Engineering and Bioengineering, Washington State University, Pullman, WA 99164, United States.

aromatic ring in the GUA conversion. A ~38% selectivity to benzene/toluene was achieved under the best reaction conditions [46]. While the transalkylation activity of the acidic catalyst offers a way to preserve the carbon from being lost as a gas product, the presence of acidic sites interacts strongly with the phenolic compounds, resulting in rapid catalyst deactivation by coking [1,9]. Contrary to the acidic supports, carbon-supported catalysts showed a much higher stability in the HDO of phenolic compounds [9].

In this study, guaiacol was used as a model compound since it is stable under the biomass fast pyrolysis conditions and has the characteristic bonds of phenolic compounds. We compared the vapor-phase HDO of guaiacol on a variety of supported metal catalysts (Pd, Pt, Ru, Fe, Cu, and PdFe). In all cases, activated carbon was used to minimize the support effect on the HDO reactions. We found that Fe/C shows promising HDO activity without saturation of the aromatic ring, forming benzene, toluene, TMB, phenol, and o-cresol as major products. A significant improvement in HDO activity was observed on the palladium-promoted Fe/C catalysts. Scanning transmission electron microscopy (STEM) imaging complemented by energy dispersive spectroscopy (EDS) showed the modification of Fe nanoparticles by Pd. Results from temperature-programmed reduction (TPR), extended X-ray absorption fine structure (EXAFS), and theoretical calculations further confirmed the strong interaction between Pd and Fe, which is responsible for the enhanced catalytic performance in the HDO of guaiacol on the PdFe/C catalysts.

2. Experimental methods

2.1. Materials and synthesis

Coconut shell activated carbon (TA70) was obtained from PICA, Inc. Acetone (99.9+%) and the metal precursors ($\text{Fe}(\text{NO}_3)_3 \cdot 9\text{H}_2\text{O}$ (98+%), $\text{Cu}(\text{NO}_3)_2 \cdot 2.5\text{H}_2\text{O}$ (99.9+%), $\text{Pd}(\text{AC})_2$ (99.9+%), $\text{Pt}(\text{NH}_3)_4(\text{NO}_3)_2$ (99.995%), Ruthenium (III) nitrosyl nitrate in nitric acid solution (1.5 wt%Ru)) were purchased from Sigma–Aldrich.

TA70-supported metal catalysts were prepared using the method of traditional incipient wetness impregnation. Specifically, a calculated amount of metal precursor was first dissolved into a given amount of H_2O (for the synthesis of Pd/C and PdFe/C, acetone was substituted for the H_2O to dissolve the palladium acetate) and then impregnated onto the support with single- or multi-impregnations to achieve the desired metal loadings of 5 wt% for Pd, Pt, and Ru, and 10 wt% for Cu and Fe. The wet solids were dried at 80 °C overnight in air and then calcined at 350 °C for 2 h (ramping rate of 5 °C/min) under flowing Ar (50 SCCM). For the 2 wt% Pd–10 wt% Fe/C, a two-step sequential incipient wetness method was used. An iron precursor solution was first impregnated on TA70, dried at 80 °C overnight, and calcined at 350 °C in flowing Ar (50 SCCM) for 2 h, followed by impregnation with the Pd precursor solution, drying at 80 °C overnight, and a second calcination step at 350 °C. Calcination at 350 °C in flowing Ar (50 SCCM) was used to decompose the metal precursors. The details of the samples and the notions are summarized in Table 1.

2.2. Characterization

XRD patterns were collected on a Philips X'pert MPD (Model PW 3040/00) equipped with a $\text{Cu K}\alpha$ X-ray source operating at 40 kV and 50 mA. Step-sizes of 0.015–0.02 and accumulation times of 0.8–1 s were used during the scanning. Nitrogen adsorption–desorption isotherms were recorded on a Quantachrome Autosorb 6-B gas sorption system. Before adsorption analysis, samples were degassed at 250 °C for 2 h. TEM images were recorded on a

Table 1

Notion and physical properties of the carbon-supported metal catalysts.

Sample information	Sample name	BET surface area (m^2/g)	Particle size (nm) ^a
TA70	C	1479	– ^b
10 wt% Fe/C	10Fe/C	1159	24.0 (± 1.6)
10 wt% Cu/C	10Cu/C	1210	11.6 (± 0.5)
5 wt% Pd/C	5Pd/C	1379	3.3 (± 0.4)
2 wt% Pd 10 wt% Fe/C	2Pd10Fe/C	1208	32 (± 1.7)
5 wt% Pt/C	5Pt/C	1361	– ^b
5 wt% Ru/C	5Ru/C	1207	– ^b

^a Particle size calculated from the XRD spectra using the Scherrer equation.

^b Below detection limit.

JEOL-2010 transmission electron microscope. STEM was performed with an FEI Titan operated at 300 kV. The FEI Titan is equipped with a CEOS GmbH double-hexapole aberration corrector for the probe-forming lens, which allows imaging at a resolution of ~0.1 nm in STEM mode. The images were acquired on a High Angle Annular Dark Field (HAADF) with an inner collection angle of 52 mrad. Compositional analysis was performed with EDAX Si (Li) energy dispersive spectroscopy (EDS) detector and FEI's TIA acquisition and analysis software. The TEM sample preparation involved the mounting of powder samples on copper grids covered with lacey carbon support film and loading into the microscope. Before XRD and TEM characterization, samples were first reduced in H_2/N_2 (1:9 mol; 50 SCCM) at 450 °C with a ramping rate of 5 °C/min for 2 h followed by purging with N_2 for 30 min, the same pretreatment procedure as those used before activity testing, and then cooled down to room temperature and passivated (0.1% O_2 in Ar and He (9:1 mol), 3 h). H_2 -TPR was conducted on a Micromeritics AutoChem II 2920 Chemisorption Analyzer equipped with a TCD detector. 100 mg of sample was loaded in a U-shaped quartz reactor and purged with flowing He (50 SCCM) until a stable base line was reached. The sample was then ramped to a given temperature at a ramping rate of 10 °C/min under flowing 10% H_2/He (50 SCCM). It was found that the temperature where noticeable loss of carbon support by hydrogenation was ~500 °C for noble metals, while it was ~600 °C for base metals or 2Pd10Fe/C in this study, verified by our H_2 -TPR-MS experiments (data not shown).

The 2Pd10Fe/C catalyst was characterized at the Pd K-edge using an in-house built, *in situ* X-ray absorption spectroscopy (XAS) cell with a 4 mm i.d. glassy carbon tubing [47]. The XAS measurements were performed at beamline X-18A at the National Synchrotron Light Source (NSLS) operated by the Synchrotron Catalysis Consortium (SCC) at Brookhaven National Laboratory. The catalyst was reduced in 100% H_2 flow (50 SCCM) at 450 °C with a ramping rate of 10 °C/min for 2 h and then cooled down to room temperature. The extended X-ray absorption fine structure (EXAFS) spectra were collected at room temperature under 100% H_2 flow. EXAFS data processing and analysis was performed using the Athena and Artemis programs of the IFEFFIT data analysis package [48,49]. Three scans were collected and merged after being aligned using a Pd foil spectrum collected simultaneously for each scan. After the normalization of the absorption coefficient, the smooth atomic background was subtracted using the AUTOBKG code to obtain $\chi(k)$ (where k is the photoelectron wave number). The theoretical EXAFS signal for Pd–Pd and Pd–Fe scattering paths was constructed using the FEFF6 code [50]. For Pd–Pd, we used an fcc crystal structure with a lattice constant of 3.89 Å. The Pd–Fe structure was constructed by replacing all the Pd atoms in the first shell of the Pd fcc structure by Fe atoms and changing the lattice constant to 3.7 Å. The theoretical EXAFS signals were fitted to the data in r -space using the Artemis program of the IFEFFIT package. The

spectra were fitted by varying the coordination number of the single scattering Pd–Pd and Pd–Fe paths, $N_{\text{Pd-Pd}}$, $N_{\text{Pd-Fe}}$, the bond length disorder (Debye–Waller factor), $\sigma_{\text{Pd-Pd}}^2$, $\sigma_{\text{Pd-Fe}}^2$, the effective Pd–Pd and Pd–Fe scattering lengths ($R_{\text{Pd-Pd}}$, $R_{\text{Pd-Fe}}$), and the correction to the threshold energy, ΔE_0 (same for both Pd–Pd and Pd–Fe). S_0^2 (the passive electron reduction factor) was obtained by first analyzing the spectrum for a Pd foil, and the best fit value (0.86) was fixed during the fitting. The k-range used for Fourier Transform of the $\chi(k)$ was 2.5–13 Å^{−1} and the r-range for fitting was 1.5–3.1 Å.

2.3. Catalyst activity measurements

Catalytic reactions were conducted in a micro-tubular fixed-bed reactor under ambient pressure with the details being provided elsewhere [51]. Briefly, a 100 mg sample (60–100 mesh) was loaded and sandwiched by two layers of quartz wool. A thermocouple was placed in the middle of the catalyst bed to monitor the reaction temperature. Before the reaction, catalysts were first reduced in H₂/N₂ (1:9 mol; 50 SCCM) at 450 °C with a ramping rate of 5 °C/min for 2 h followed by purging with N₂ for 30 min. A reduction temperature of 450 °C was used to reduce metal oxides while minimizing the gasification of the carbon support based on separate TPR results (not shown). The HDO reaction was then conducted by using a syringe pump (Core Parmer 74900) to introduce guaiacol into a vaporizer (190 °C) where it is then carried into the reactor by the flowing H₂/N₂ gas. The purity of all gases used was 99.999%. The guaiacol and hydrogen partial pressures within the reactor were controlled by adjusting the relative flow rates of the gases and liquid feed streams. The product line was heated at ~190 °C before the cold trap to avoid the condensation of liquid products. A Shimadzu 2400 Gas Chromatography (GC), equipped with an auto sampling valve, RTX (30 m, 0.53 mm, 0.5 μm) column, Flame Ionization Detector (FID), was connected to the line between the reactor outlet and cold trap to collect and analyze the products in the effluent gas. After the cold trap, the dry gas was sent to an online micro GC for the analysis of gas products (i.e., CH₄, CO₂, CO, C₂H₆, N₂, and H₂). Nitrogen was used as the internal standard for the micro GC. Response factors for guaiacol and the HDO reaction products were determined using pure compounds with known concentrations. The C mass balance, unless otherwise noted, was at least 95%. Guaiacol conversion (X_{guaiacol}), products selectivities ($S_{\text{products-i}}$), and product yields ($Y_{\text{products-i}}$) were calculated as follows: $X_{\text{guaiacol}} = (\text{Mol}_{\text{guaiacol-in}} - \text{Mol}_{\text{guaiacol-out}}) / \text{Mol}_{\text{guaiacol-in}}$; $S_{\text{products-i}} = (\text{Mol}_{\text{product-i}} \times \alpha_i) / (\text{Mol}_{\text{reacted guaiacol}} \times 7)$, α_i refers to the carbon number in product-i; $Y_{\text{products-i}} = X_{\text{products-i}} \times S_{\text{products-i}}$. The conversion, selectivities, and yields are reported as the average over 1 h at each temperature. All catalysts showed signs of deactivation. Therefore, the data reported were limited to the first 120 min of time-on-stream during which the deactivation (estimated by the drop in guaiacol conversion), unless otherwise mentioned, was minimal (<10%).

3. Computational details

Density functional theory (DFT) calculations were performed with the Vienna *Ab initio* Simulations Package (VASP) code [52,53]. The projector augmented-wave (PAW) method [54] for the electron-ion interactions and the generalized gradient approximation (GGA) using the Perdew–Wang-91 (PW91) [55] functional were employed for the treatment of the exchange–correlation effects. With its PAW potentials, VASP combines the accuracy of all-electron methods with the computational efficiency of plane-wave approaches. The electronic wave functions were expanded in a basis set of plane waves with kinetic-energy cutoffs of 400 eV and 440 eV for the Pd and Fe host systems, respectively.

The lattice constant of both bulk Fe and bulk Pd was calculated to be 2.827 Å and 3.957 Å, respectively. These lattice constants are in good agreement with the literature, where theoretical values of 2.834 Å [56] and 3.96 Å [57] were reported. They were obtained by sampling the corresponding primitive body centered cubic cell (Fe) and the primitive face centered cubic unit cell (Pd) with a (12 × 12 × 12) **k**-points Monkhorst–Pack grid.

In order to study the surface properties of the PdFe catalyst, two different configurations of an Fe, or Pd, impurity in a Pd(111), or Fe(110), host surface were examined. The first configuration had a single pure impurity layer while the second examined a perfectly mixed scenario within the top two layers (see Fig. 1). The two possible host surfaces were modeled with two $p(4 \times 4)$ supercells that were 6 layers thick. The vacuum thickness within these cells was 16 Å for the Pd(111) host and 12 Å for the Fe(110) host. The host atoms in the bottom two layers of the super cell were kept fixed at their bulk positions, and all other atoms were allowed to relax. These unit cells were sampled with a (3 × 3 × 1) **k**-points Monkhorst–Pack grid. A Methfessel–Paxton smearing of 0.1 eV was used to improve the convergence and the total energy was extrapolated back to zero Kelvin. Spin-polarization effects were found to have a significant effect on the energy differences and were taken into account appropriately. Dipole corrections [58] to the electrostatic potential and total energy were imposed to eliminate dipole–dipole interactions of images between the super cells. Finally, the total energy convergence threshold was set to 10^{−4} eV and the geometries were considered to be fully relaxed when the forces were less than 0.03 eV/Å.

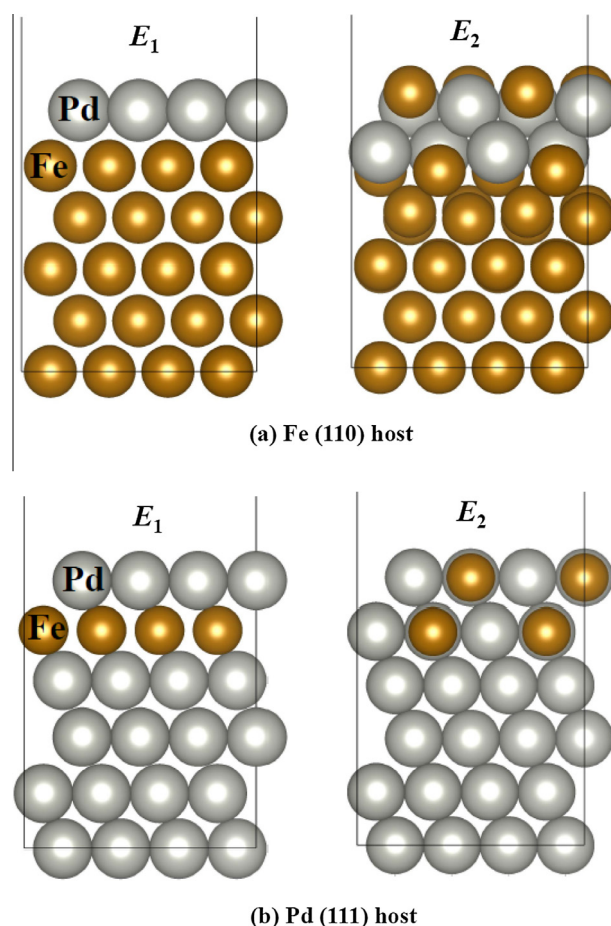


Fig. 1. Structures of: (a) a Pd layer in the Fe(110) surface host; and (b) an Fe layer within the Pd(111) surface host.

The surface segregation energy was defined as the energy difference: $\Delta E = E_1 - E_2$, where E_1 refers to the total energy of the system with a single pure impurity layer and E_2 refers to the energy of the perfectly mixed scenario within the top two layers of the host metal. With this definition, if the surface segregation energy is negative (positive), the pure layer (mixed) configuration will be more stable.

Calculations modeling the adsorption of phenol on a model PdFe surface were performed using $p(4 \times 4)$ supercells. The near surface was modeled using a four layer slab with the bottom two layers being fixed in their bulk positions. The plane-wave basis set was expanded to a kinetic energy of 400 eV and 10 Å of vacuum was present between the phenol adsorbate and repeating supercells. All other calculation parameters and convergence criteria were kept consistent from the surface segregation calculations. The strength of each of these adsorption configurations was evaluated using the below definition for the adsorption energy.

$$E_{\text{ads}} = E_{\text{Phenol+Surface}} - E_{\text{Phenol}} - E_{\text{Surface}} \quad (1)$$

The more negative the calculated adsorption energy, the stronger and more favorable the adsorption of phenol.

4. Results and discussions

4.1. Catalysts characterization

BET surface areas of the calcined catalysts were determined by nitrogen sorption and are summarized in Table 1. The carbon support has a surface area of $\sim 1480 \text{ m}^2/\text{g}$. After loading with the metals, all the catalysts showed slightly decreased surface areas as expected.

In Fig. 2, TEM imaging of the fresh (reduced and passivated) catalysts reveals that all the precious metal catalysts have a uniform distribution of small particles ($< 5 \text{ nm}$ in size). The Pt- and Ru-supported catalysts showed the smallest particle size ($< 2 \text{ nm}$) while the Pd particle size was slightly larger ($2\text{--}5 \text{ nm}$). In contrast to the supported precious metals, the 10Fe/C (Fig. 2) and 10Cu/C (Fig. S1) catalysts had a broad distribution of particle sizes. Although most of the particles were in a size range between 1 and 5 nm, large particles from 20 to 100 nm were also observed, which can be related to the higher metal loadings in these catalysts. XRD patterns of the fresh 5Pd/C, 10Cu/C, 2Pd10Fe/C, and 10Fe/C samples show typical diffractions of corresponding Pd, Cu, and Fe metals (Fig. S2). Based on the Scherer equation, the average particle sizes were 24.0 nm, 12.0 nm, and 3.3 nm for 10Fe/C, 10Cu/C, and 5Pd/C, respectively. The large average particle size obtained from XRD for the 10Fe/C and 10Cu/C confirms the broad particle size distribution observed by TEM. The Pt and Ru particle sizes could not be calculated since the peak corresponding to the (111) lattice spacing was very broad and could not be reliably differentiated from the background which is in agreement with the 1–2 nm particles seen in the TEM images (Fig. 2). The 2Pd10Fe/C showed Fe particle size of 31.9 nm (from XRD, Fig. S2) which is slightly larger than that for 10Fe/C (24 nm, Table 1). Since 2Pd10Fe/C was prepared by impregnating 10Fe/C with Pd precursor, we would expect that both 2Pd10Fe/C and Fe/C have a similar metallic Fe particle size. The minor difference observed could be due to a thinner Fe oxide shell formed in the presence of Pd during passivation. No diffraction corresponding to Pd or PdFe alloy phase were resolved for the 2Pd10Fe/C sample (Fig. S2).

To further study the structure of 2Pd10Fe/C catalyst, we characterized the catalyst using STEM imaging complemented by EDS. Similar to the 10Fe/C catalyst, particles with a bi-modal size

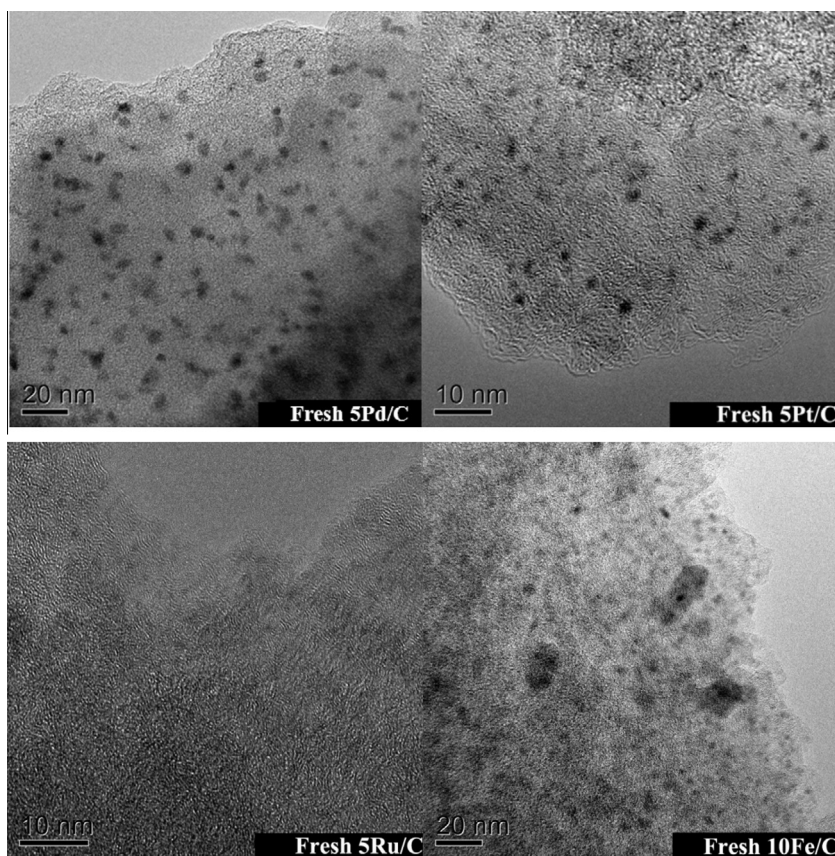


Fig. 2. TEM images of the carbon-supported catalysts.

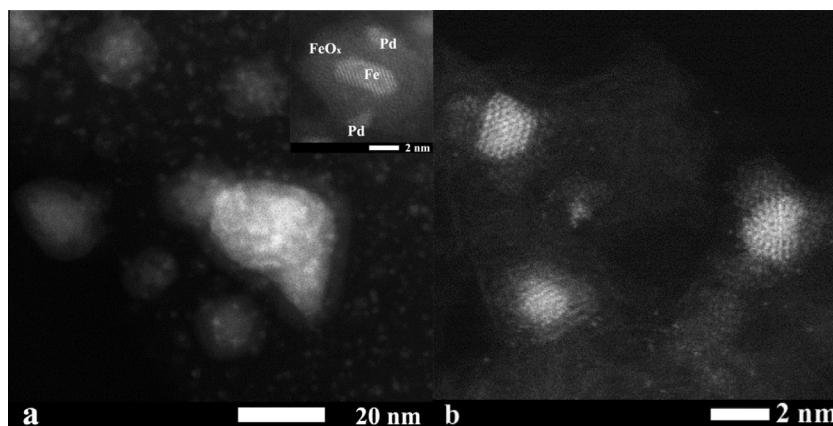


Fig. 3. (a) HAADF STEM image revealing the presence of larger Fe/FeOx core-shell particles enriched with small patches of Pd and much smaller Pd–Fe nanoparticles (sample 2Pd10Fe/C); (b) detailed view of the small Pd–Fe nanoparticles.

distribution were observed, as seen in Fig. 3a. The smaller nanoparticles, which are present in a much higher number density, were identified by EDS as either palladium-enriched iron or iron-enriched palladium. This is possibly due to the formation of PdFe alloys with different compositions (Fig. S3). The bigger irregular-shaped particles seen in Fig. 3a are iron with the dark shell structure around them being iron oxide (the oxide being formed by room temperature passivation (0.1% O₂/Ar)). Notably, brighter nano-dots are clearly present on the bigger iron particles. A close study with single-spot EDS analysis indicated that the brighter spots are palladium in contact with the larger iron particles (Fig. S3). Fig. 3b shows a higher magnification STEM image of the smaller nanoparticles. It can be seen that the particles consist of a Pd core with a shell of iron oxide, suggesting that the Pd and Fe are in close contact with the same particle. However, for such small particles (1–2 nm), the segregation of Fe to the surface would be expected as the sample is oxidized upon exposure to air during the TEM sample preparation. EDS spectra of larger and smaller particles also show different Pd and Fe compositions (Fig. S3).

TPR experiments were performed to further confirm the strong interaction between Fe and Pd as shown in Fig. 4. Since palladium oxide can be readily reduced at room temperature [59], the TPR experiment was started at –15 °C. No clear hydrogen consumption was observed for 5Pd/C below 200 °C, and instead, a larger hydrogen release peak centered at 53 °C was detected, which is due to the decomposition of palladium hydride (PdH_x) [59–61].

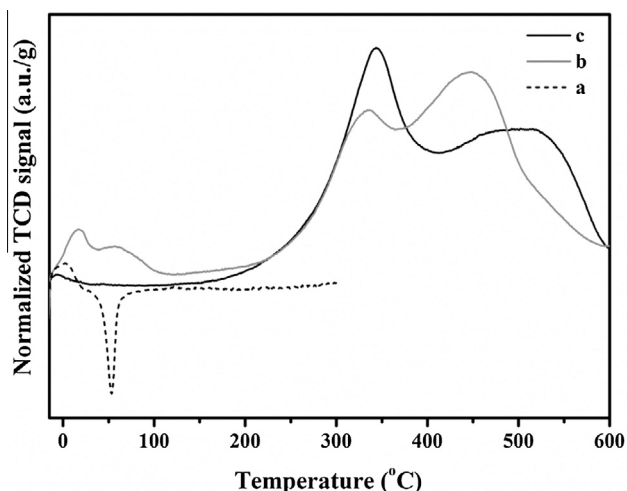


Fig. 4. H₂-TPR profiles of: (a) 5Pd/C, (b) 2Pd10Fe/C, (c) 10Fe/C.

The β -PdH_x phase has been reported to decompose in the range of 65–85 °C for Pd/SiO₂ [60] and in the range of 54–75 °C for Pd/C [59] depending on the particle size and stoichiometry of the hydride. The smaller the particles, the lower the stoichiometry and decomposition temperature [59,60,62]. It is clear that the palladium oxide nanoparticles in our 5Pd/C catalyst can be readily reduced at a temperature as low as –15 °C. On the calcined 10Fe/C, two hydrogen consumption peaks (340 °C and 520 °C) were observed, which are associated with the reduction of Fe³⁺ and Fe²⁺, respectively. Over the 2Pd10Fe/C catalyst, hydrogen consumption was observed between –15 °C to 100 °C, which is different from that of 5Pd/C catalyst. No H₂ release peak (negative peak) was observed which could be due to the PdFe alloy formation or due to being masked by the large consumption peak. Moreover, the hydrogen consumption peaks corresponding to the reduction of Fe³⁺ and Fe²⁺ between 300 °C to 550 °C shifted to lower temperatures due to the presence of Pd. Overall, it is most likely that the H₂ consumption between –15 °C and 100 °C is due to the reduction of the small Pd–Fe nanoparticles, while the peaks at higher temperatures are likely due to the large Fe-rich particles.

In order to confirm whether Pd and Fe formed an alloy as suggested by TPR and STEM/EDS, we characterized the 2Pd10Fe/C catalyst using EXAFS. Fig. 5 shows the magnitude of k²-weighted

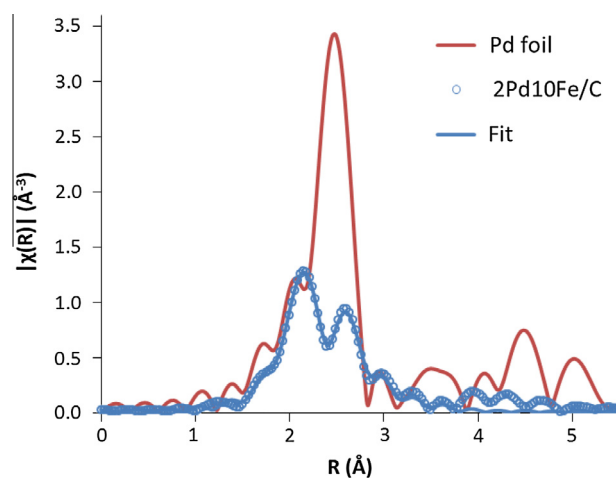


Fig. 5. Magnitude of k²-weighted Fourier transform of Pd K-edge EXAFS data for the 2Pd10Fe/C (blue, open circles), fit (blue line) and Pd foil (red line). The k-range for the Fourier Transform was 2.5–13 Å^{−1}. The catalyst was reduced at 450 °C in 100% H₂ for 2 h and then cooled to room temperature prior to the EXAFS data scans. (For interpretation of the references to color in this figure legend, the reader is referred to the web version of this article.)

EXAFS Pd K-edge spectra for a Pd foil, 2Pd10Fe/C catalyst under 100% H₂ at room temperature, and the fit for 2Pd/10Fe/C. It can be seen from Fig. 5 that the spectrum for 2Pd10Fe/C differs significantly from that of a monometallic Pd with the appearance of a peak at 2.15 Å (not phase corrected), suggesting the formation of PdFe alloy. The data and fit using Pd–Pd and Pd–Fe scattering paths are also shown in *r*-space in Fig. 5 and the fitting results are listed in Table 2. The Pd–Pd bond distance (2.726 Å) was significantly shorter than bulk Pd (2.751 Å), especially considering that the spectrum was collected under 100% H₂ which would promote the formation of Pd-hydride and increase the Pd–Pd bond distance. In addition, the fitted Pd–Fe coordination number was 2.7 and the Pd–Fe bond distance (2.608 Å) was significantly shorter than that of Pd–Pd (2.726 Å). These results clearly show that Pd formed an alloy with Fe which confirms the STEM/EDS and TPR results. Further information on the structure of the nanoparticles from the EXAFS results cannot be extracted due to the broad particle size and composition distributions (from STEM/EDS).

DFT calculations were used to better understand the interaction between Pd and Fe. It has been reported that Pd presents a strong surface segregation preference when acting as an atom impurity within a Fe host while a Fe impurity atom within a Pd host shows a preference for strong anti-segregation [63,64]. From this, it is expected that when the host material in a PdFe alloy is either Fe or Pd, the surface composition will tend to favor an enrichment of Pd. However, no theoretical work has been undertaken to determine if the surface segregation behavior is enhanced or inverted when examining a layer of one type of metal as an impurity in the other as a host. To this end, two configurations for the Fe(110) surface were constructed. One scenario had a pure Pd top layer and the other had a perfectly mixed PdFe alloy within the top two layers, as shown in Fig. 1a. The surface segregation energy for the Fe(110) host system, as defined in Section 3, was found to be –0.275 eV/Pd, which implies that Pd atoms prefer to form a pure layer on the surface of the Fe(110) host rather than mixing itself with the subsurface Fe atoms. This observation is in line with our STEM/EDS observations on large-sized Fe particles (20–30 nm). Similar calculations were performed with the Pd(111) surface acting as the host material. Because the Fe impurity within a Pd host shows a strong tendency toward anti-segregation, the Fe impurity layer will prefer to be located somewhere within the host material, away from the surface. However, nothing is known about the preferred Fe layer location within the subsurface Pd layers. Therefore, the most favorable subsurface layer in which to place a pure Fe layer had to be determined. Calculations were performed with the pure Fe layer in different layers within the Pd(111) host, and these results showed that the most stable configuration for the pure Fe layer was when it was placed in the second layer of the Pd(111) host (see supporting materials). This preferential configuration for the pure Fe layer within the Pd host was then compared with a perfectly mixed system as examined for the Fe(110) host case above. These configurations are shown in Fig. 1b. For the Pd host situation, the surface segregation energy was found to be –0.286 eV/Fe, showing that Fe atoms prefer to form a pure layer in the second layer of Pd(111) surface. The surface segregation results presented above confirm that the surface of the PdFe alloy will be enriched in Pd with Fe beneath. These observations differ somewhat to the STEM/EDS results for the very

small particles (2–3 nm) with Pd as host, in which Pd core and Fe₂O₃ shell structure were observed. This could be due to the oxidation of Fe which migrates to the surface of Pd under air during STEM sample preparation.

To summarize, STEM characterizations showed that the 2Pd10Fe/C catalyst has both larger Fe particles modified by Pd patches and smaller Pd–Fe nanoparticles without monometallic Pd or isolated Fe being observed. The results from TPR, STEM/EDS, and EXAFS characterization reveal the formation of Pd–Fe alloy for the 2Pd10Fe/C catalyst. Finally, DFT calculations suggest that the surface of Pd–Fe alloy is enriched in Pd and the subsurface is enriched in Fe.

4.2. Hydrodeoxygenation of guaiacol

The supported metal catalysts were evaluated at temperatures from 250 °C to 450 °C under atmospheric pressure. Blank-reactor showed a negligible activity for guaiacol at temperatures below 350 °C. When the reaction temperature is increased from 350 to 450 °C, the conversion of guaiacol to catechol is observed. However, this conversion was still very low, increasing from 0.2% to 6.3% with negligible deoxygenated products being formed (Table S1). The pure carbon support also showed negligible activity at 250 °C, but became significantly more active at higher temperatures, e.g., reaching 29.1% and 65.1% guaiacol conversions at 350 °C and 450 °C, respectively. The major products with this catalyst were found to be catechol and phenol (Fig. S4). Separate experiments at low conversions on the carbon support (data not shown) showed that catechol is the primary product formed via demethylation of guaiacol, while phenol was a secondary product formed by HDO of catechol. This observation suggests the facile demethylation of guaiacol in the absence of metal catalysts, consistent with the weaker Me–OAr bond strength (247 kJ/mol, demethylation) compared with the C_(Ar)–OMe bond (356 kJ/mol, demethoxylation) in the guaiacol molecule [12]. Therefore, although the carbon support is active in converting guaiacol to catechol and phenol at 350–450 °C, it does not further catalyze the deoxygenation of phenol as evidenced by the lack of benzene and toluene/trimethylbenzene (TMB) produced at these temperatures.

The acidity of the support has been found to have a key effect on the reaction of methyl substitution in HDO of guaiacol [17,19,42]. In this study, no detectable methylated guaiacol and only very small amounts of cresol were observed. This is most likely due to the significantly lower acidity of the carbon support when compared with the acidity of metal oxide supports like Al₂O₃ and H-beta [17–19]. These acidic, metal oxide supports can cause both unimolecular and biomolecular transalkylation as well as HDO by the metal catalysts, resulting in various methylated products such as cresol, methylated guaiacol, toluene, and trimethylbenzene.

4.2.1. Carbon-supported precious metal catalysts

The carbon-supported metal catalysts exhibited significant activity and yields to deoxygenated products (i.e., phenol, oxygen-free aromatic compounds, cyclohexanone, and cyclohexanol) as shown in Fig. 6 and Table S2. Among the monometallic precious metal catalysts at 250 °C (Fig. 6A), catalyst activity (as measured by guaiacol conversion) increased in the order of: 5Pd/C (50.4%) < 5Pt/C (87.7%) < 5Ru/C (95.5%). Phenol was the major

Table 2
EXAFS fitting results for the 2% Pd–10% Fe/C catalyst at the PdK edge. EXAFS spectra were collected at 25 °C in 100% H₂ flow. The numbers in parentheses indicate the statistical error in the most significant digit obtained from the fit in Artemis (e.g., 5.2(7) = 5.2 ± 0.7).

	$N_{\text{Pd-Pd}}$	$R_{\text{Pd-Pd}}$ (Å)	$\sigma^2_{\text{Pd-Pd}}$ (Å ²)	$N_{\text{Pd-Fe}}$	$R_{\text{Pd-Fe}}$ (Å)	$\sigma^2_{\text{Pd-Fe}}$ (Å ²)	ΔE_0 (eV)	Reduced χ^2
2Pd10Fe/C	5.2(7)	2.726(5)	0.009(2)	2.7(6)	2.608(7)	0.005(2)	1.7(5)	9.7

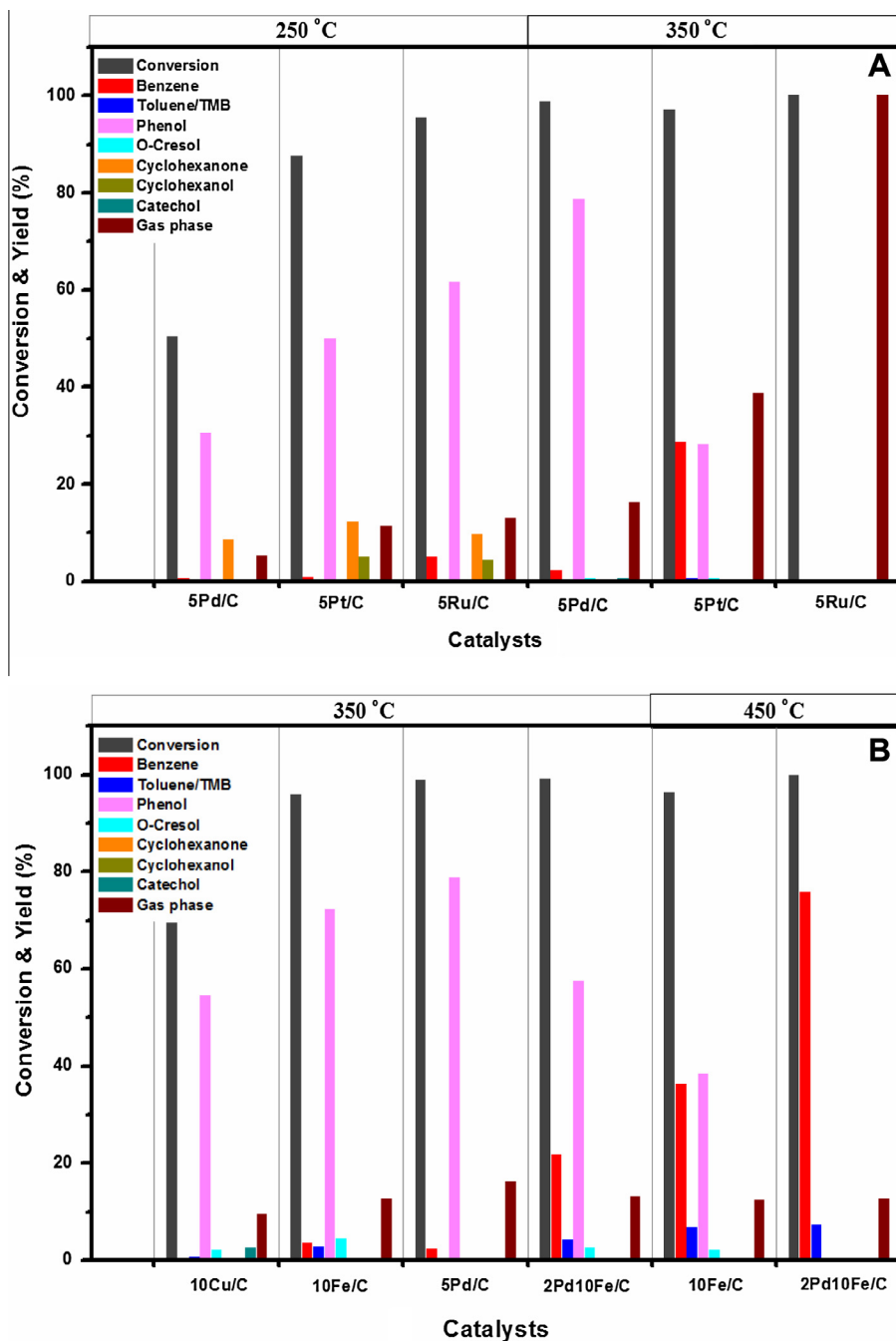


Fig. 6. Product distribution in HDO of guaiacol at different temperatures on (A) precious catalysts; and (B) base metal and bimetallic catalysts (for comparison purposes, 5Pd/C was included in (B)). 100 mg catalyst, $P_{\text{guaiacol}} = 0.4$ kPa; $P_{\text{H}_2} = 40$ kPa, W/F = 0.15 s.g. STP mL⁻¹.

product with its yield increasing in the order of: 5Pd/C (30.6%) < 5Pt/C (50.0%) < 5Ru/C (61.6%). In addition, an appreciable amount of benzene (up to 5% yield) and aromatic ring saturated products such as cyclohexanone (~10% yield) and cyclohexanol (up to 5% yield) were also observed on 5Pd/C, 5Pt/C, and 5Ru/C (Fig. 6A). As exemplified over the Ru/C catalyst (Fig. 7), separate experiments at 250 °C revealed that the selectivities to benzene, cyclohexanone, and cyclohexanol increased at the expense of phenol with the increasing residence time, suggesting that benzene was formed via hydrodeoxygenation of phenol while cyclohexanone and cyclohexanol were formed via the parallel aromatic ring saturation of phenol on these precious metal catalysts.

Upon increasing the reaction temperature to 350 °C, no ring-saturation products (cyclohexanone/cyclohexanol) were observed on 5Pd/C, 5Pt/C and 5Ru/C, and yields to gas-phase products (mainly C1 products including methane, CO, and CO₂) increased in the order of: 5Pd/C (16.2%) < 5Pt/C (38.8%) < 5Ru/C (100%) (Fig. 6A). The yields to C1 products were above the theoretic yield (~15%) if only demethylation and/or demethoxylation of guaiacol took place. These results suggest that the aromatic ring saturation of phenol and the subsequent ring opening to form C1 gas products are facile on precious metal catalysts at 350 °C. Compared to the results at 250 °C, the yield to benzene was higher on 5Pd/C and 5Pt/C but no benzene was observed on 5Ru/C at 350 °C. This implies that a parallel benzene hydrogenation [65], followed by ring

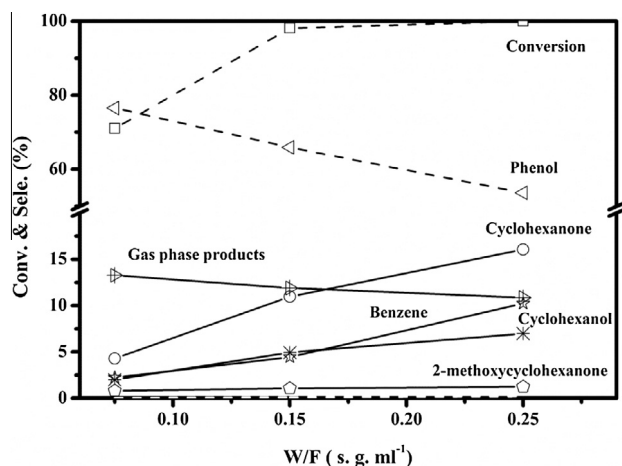


Fig. 7. Products distribution in HDO of guaiacol as a function of residence time on 5Ru/C. 100 mg, $P_{\text{guaiacol}} = 0.4$ kPa; $P_{\text{H}_2} = 40$ kPa, $T = 250$ °C.

opening to form C1 products, is prevalent on these catalysts. These results also suggest that Ru was the most active, while Pd was the least active catalyst for ring opening among Ru, Pt, and Pd catalysts as evidenced by 100% yield to gas-phase products for 5Ru/C as opposed to 16.2% and 38.8% for 5Pd/C and 5Pt/C, respectively, at 350 °C. Consistent with our observations, Elliott et al. also observed significant gasification on Ru/C in HDO of guaiacol in a high-pressure batch reactor (~ 7 MPa) at ≥ 250 °C [20]. Additional experimental results on 5Ru/C and 5Pt/C (data not shown) revealed that although the ring-opening reactivity can be lowered by increasing the space velocity, carbon–carbon cleavage is unavoidable on the carbon-supported precious metal catalysts. Along with the different ring-opening reactivity, the deoxygenation activity also varied from metal to metal. The deoxygenation activity at 250 °C, measured as the yield to all deoxygenated products, as seen in Fig. 8, decreased in the order of: 5Ru/C (61.9%) > 5Pt/C (50.4%) > 5Pd/C (30.8%). The lower deoxygenation activity of the Pd catalyst is also evidenced at 350 °C, where phenol was the major product (78.8% yield). In summary, the results suggest that precious metals are poor catalysts for the vapor-phase HDO of guaiacol due to their ring-saturation and ring-opening activity.

As one of the compounds from the pyrolysis of lignin [5], guaiacol has been studied extensively as a representative molecule in the HDO of pyrolysis oil. A variety of supported precious metal catalysts have been evaluated, and it is widely accepted that the hydrogenation reaction pathway is favored at low temperatures [20,33,34]. Hydrogenation of the aromatic ring in guaiacol (with 2-methoxycyclohexanone and 2-methoxycyclohexanol products), followed by a demethoxylation and/or dehydroxylation pathway (with cyclohexanone/cyclohexanol and cyclohexane products) have been proposed in the HDO of guaiacol on Rh-based catalysts [66]. In the current study, although our residence time experiments on 5Ru/C showed the formation of 2-methoxycyclohexanone, its selectivity showed almost no dependence on the residence time (Fig. 7). Instead, the selectivity to cyclohexanone and cyclohexanol increased at the expense of phenol, which suggests that cyclohexanone and cyclohexanol are formed from hydrogenation of phenol instead of 2-methoxycyclohexanone on Ru. On Pd/C and Pt/C, similar reaction pathways were found in this study, i.e., demethoxylation of guaiacol to form phenol takes place on the precious metal catalysts followed by hydrogenation to cyclohexanone and cyclohexanol. It should be noted that the demethylation pathway to form catechol followed by HDO to phenol cannot be excluded since the reaction was operated in an integral reactor and HDO of catechol to phenol is facile [15]. These results are also in agreement with the reaction network proposed by Nimmanwudipong et al. for the reaction of guaiacol with H_2 on Pt/ Al_2O_3 at atmospheric pressure [19]. At low guaiacol conversion, catechol and phenol were identified as the intermediates for the reactions proceeding on Pt (in contrast to the reactions on Al_2O_3), while cyclohexanone was identified as a secondary product [19]. Facile hydrogenation of phenol to cyclohexanone and cyclohexanol has also been reported by Zhao et al. on Pd/C at 250 °C and 5 MPa H_2 pressure [33].

4.2.2. Carbon-supported base metal catalysts

The activities of base metal catalysts including Fe and Cu were also studied for guaiacol conversion. As can be seen in Fig. 6B, 10Fe/C is more active than 10Cu/C at 350 °C as evidenced by guaiacol conversions of 96.0% and 69.5%, respectively, with phenol being the major product. Interestingly, both 10Fe/C and 10Cu/C catalysts showed no ring-saturation activity since no cyclohexanone

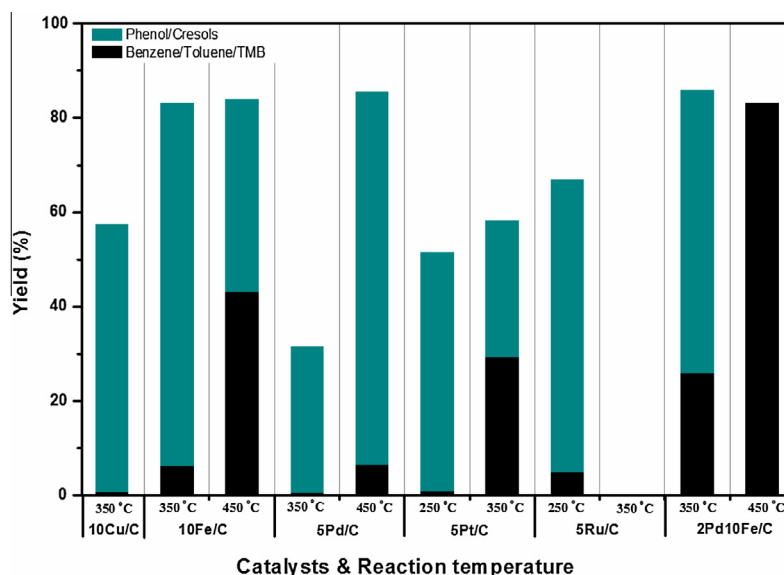


Fig. 8. Comparison of yields to oxygen free (i.e., Benzene/Toluene/TMB) and 1-oxygen aromatic compounds (phenol/cresols). 100 mg catalyst, $P_{\text{guaiacol}} = 0.4$ kPa, $P_{\text{H}_2} = 40$ kPa, $W/F = 0.15$ s.g.STP mL^{-1} .

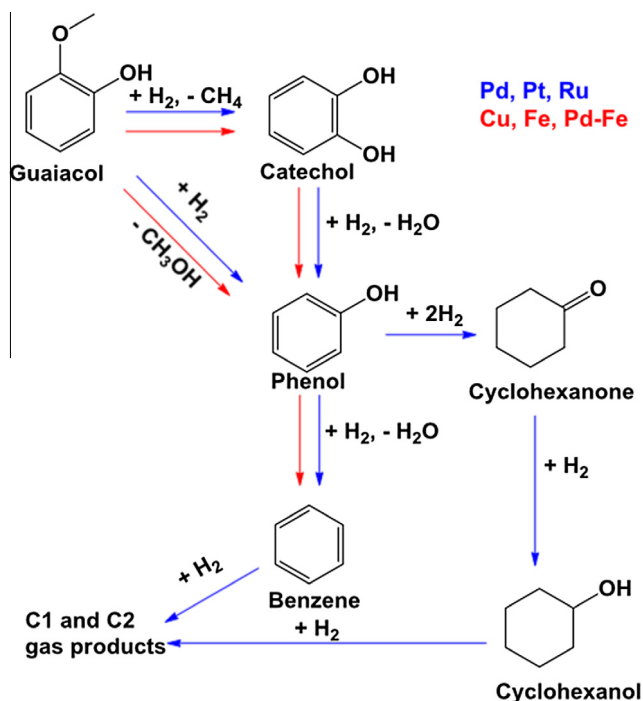


Fig. 9. Reaction pathways on precious metals (Pd, Pt, Ru) as indicated by blue arrows vs. reaction pathways on base metals (Cu, Fe) and bimetallic Pd-Fe as indicated by red arrows. (For interpretation of the references to color in this figure legend, the reader is referred to the web version of this article.)

and cyclohexanol were detected at any temperature investigated. Moreover, the selectivity to C1 products is close to that if only demethylation and/or demethoxylation of guaiacol take place (~15%). Instead, oxygen-free aromatic compounds (i.e., benzene/toluene/TMB) were found on these base metal catalysts. On Cu/C, the yield to the oxygen-free aromatic compounds was less than 1%. However, on the Fe/C catalyst at 350 °C, the yield to oxygen-free aromatic compounds (i.e., benzene/toluene/TMB) reached ~7.3% and further increased to ~43.3% at 450 °C at the expense of phenol and o-cresol (Fig. 6B). These results suggest that further deoxygenation of phenolic products is facile on the Fe/C catalyst. It should be noted that methanol was detected on both the Fe and Cu catalysts suggesting that phenol (and not catechol) is the major primary product from the deoxygenation of guaiacol. On the precious metal catalysts, no methanol was detected, which can be due to either a higher activity for methanol HDO to methane or a more competitive guaiacol demethylation pathway in parallel to the guaiacol demethoxylation pathway.

4.2.3. Carbon-supported bimetallic catalysts

Fe appears to be a very good catalyst for the HDO of guaiacol, especially in the phenol to benzene deoxygenation step which proceeds without the presence of the ring-saturation side reaction (Table S2). However, its activity is lower than the precious metal

catalysts. Among the precious metals, Pd appeared to show no significant ring-opening activity. To further improve the activity of Fe catalyst, a Pd-promoted Fe catalyst was explored. As shown in Fig. 6B, 2Pd10Fe/C catalyst exhibited a significantly improved yield to oxygen-free aromatic compounds (benzene/toluene/TMB) than 10Fe/C and 5Pd/C at 350 °C. Specifically, 25.9% yield to the oxygen-free aromatic compounds was observed on 2Pd10Fe/C as opposed to 6.3% for 10Fe/C and 2.7% for 5Pd/C as shown in Fig. 8. At 450 °C, on the PdFe/C catalyst, the phenolic compounds were fully deoxygenated on PdFe/C and the yield to oxygen-free aromatic compounds (benzene/toluene/TMB) reached 83.2% as opposed to the 43.3% observed on 10Fe/C. It should be noted that small amounts of biphenyl were also detected (~5% yield). Similar to the 10Fe/C, methanol was also detected on the 2Pd10Fe/C catalyst, suggesting that phenol was formed primarily via demethoxylation of guaiacol. In addition, no aromatic ring-saturation products such as cyclohexanone and cyclohexanol were observed. The yield to C1 gas products at 350 and 450 °C is close to the theoretical yield if only demethylation and/or demethoxylation of guaiacol takes place (~15%), indicating there is no aromatic ring opening on the 2Pd10Fe/C catalyst. For a direct comparison of the overall HDO activity, the yields to oxygen free (i.e., benzene/toluene/TMB) and 1-oxygen containing aromatic compounds (phenol and cresol) of the catalysts were plotted and compared in Fig. 8, which clearly shows the significant improvement of HDO activity on the 2Pd10Fe/C catalyst compared with monometallic precious or base metal catalysts.

From the aforementioned results, it is clear that the reaction pathways for guaiacol HDO (based on the major products) are highly dependent on the type of catalyst. Fig. 9 shows the proposed reaction pathways on the supported metal catalysts studied in this work. Over the supported metal catalysts studied here, phenol was the major intermediate formed through either demethylation of guaiacol followed by HDO of catechol or demethoxylation of guaiacol with the latter being the major pathway on Fe, Cu, and PdFe. Phenol conversion proceeded in different reaction pathways depending on the metal and reaction temperatures. Over precious metal catalysts, hydrogenation of phenol via ring saturation to form cyclohexanone and cyclohexanol and/or dehydroxylation of phenol to form benzene took place, followed by ring opening to form C1 and C2 products (CH₄, CO_x, and small amounts of C₂H₆). On the contrary, base metal catalysts (i.e., 10Cu/C and 10Fe/C) showed no measurable activity toward ring saturation or ring opening. In addition, 10Fe/C exhibited a higher hydrodeoxygenation activity than 10Cu/C, resulting in the predominant formation of benzene.

2Pd10Fe/C showed a higher and synergistic activity for HDO of guaiacol to form benzene than did either the 10Fe/C and 5Pd/C catalysts, which has never been reported. Our experimental results further revealed that guaiacol conversion to phenol is facile on the supported metal catalysts investigated, and the enhanced HDO of guaiacol on 2Pd10Fe/C is due to its high activity for HDO of phenol. To determine the active phase for the catalytic HDO of phenolic compounds on the PdFe surface, the adsorption of phenol

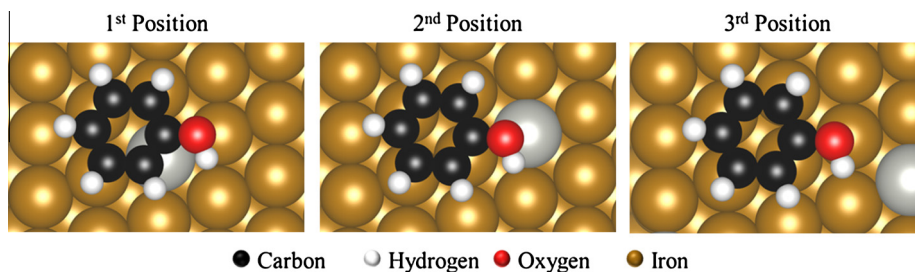


Fig. 10. Adsorption configurations of phenol on an Fe(110) surface with a surface Pd atom. The distance from the adsorbate to the Pd atom increases from position 1 to 3.

Table 3

Adsorption energies and structural deformations of phenol on Fe(110) with a Pd impurity. The distance between adsorbate and Pd impurity increases from position 1 to 3.

Position	E_{ads} (eV)	$d_{\text{C-O}}$ (Å)	$\theta_{\text{C-O}}$ (°)
Phenol gas	–	1.38	3
1st	–0.77	1.37	13
2nd	–0.91	1.38	14
3rd	–1.12	1.41	14

on an Fe(110) surface with a surface Pd atom was further studied using DFT. Three configurations of phenol with increasing distance from the adsorbate to the surface Pd atom were considered, as shown in Fig. 10. The resulting adsorption energies and structural deformations of phenol caused by the surface interaction are shown in Table 3. As the distance between the phenol adsorbate and Pd atom increases, both the adsorption energy and carbon–oxygen bond length increase. This increase in the adsorption strength of phenol with increasing distance from the Pd atom suggests that phenol adsorption is more favorable on the Fe surface of the catalyst. In addition to the increased adsorption strength on the Fe surface, the lengthening of the carbon–oxygen bond as phenol adsorbs away from the Pd atom indicates that the Fe surface interaction weakens that bond and makes the phenol more susceptible to HDO. The preferential adsorption and activation of phenol on Fe(110) suggests that the Fe is likely the active site for HDO of phenol. From the TPR results (Fig. 4), the presence of Pd facilitates the reduction of FeO_x . In addition, our STEM/EDS results clearly showed the intimate mixing of Pd and Fe, forming a Pd–Fe alloy with various compositions. The Pd–Fe alloy formation was further confirmed by EXAFS and TPR studies. DFT calculations suggest that the surface of Pd–Fe alloy is enriched in Pd with Fe beneath, consistent with the STEM observation of Pd nano-dots on Fe particles (Fig. 3a). Therefore, the presence of Pd facilitates the reduction of FeO_x and modifies Fe, leading to enhanced HDO of phenol. The presence of Pd may also facilitate H_2 dissociation/oxygen removal, which is currently under investigation. Regarding the absence of ring saturation on 2Pd10Fe/C catalyst, our DFT calculations have shown the preferential adsorption and activation of phenol on Fe, which likely prevents its hydrogenation on Pd.

5. Conclusions

HDO of guaiacol on a series of carbon-supported metal catalysts was studied under atmospheric pressure. Phenol was the major intermediate on all the metal-supported catalysts studied. Precious metal catalysts showed higher activity; however, saturation of aromatic ring and C–C bond cleavage also took place, leading to the formation of cyclohexanone, cyclohexanol, and gaseous C_1 products. Base metal catalysts, especially Fe/C, were found to have lower activity but exhibit higher hydrodeoxygenation selectivity without ring opening and ring saturation with benzene, toluene, phenol, and cresol being the major products. Bimetallic PdFe/C catalysts were found to exhibit a significantly enhanced hydrodeoxygenation activity with 83.2% yield to benzene/toluene/TMB at 450 °C, which is due to the modification of Fe by Pd as confirmed by high-resolution STEM imaging complemented by EDS, temperature-programmed reduction, EXAFS, and theoretical calculations.

Acknowledgments

We gratefully acknowledge the financial support from the National Advanced Biofuels Consortium (NABC) which is funded by the Department of Energy's Office of Biomass Program with recovery act funds. We also thank the financial support from the US Department of Energy (DOE), Office of Basic Energy Sciences,

Division of Chemical Sciences, Geosciences, and Biosciences. This work was performed in the Environmental Molecular Sciences Laboratory, a national scientific user facility sponsored by the U.S. Department of Energy's Office of Biological and Environmental Research, located at Pacific Northwest National Laboratory (PNNL) in Richland, WA. Use of the National Synchrotron Light Source, Brookhaven National Laboratory, for the EXAFS experiments was supported by the US Department of Energy, Office of Basic Energy Sciences (Grant# DE-FG02-05ER15688). The DFT calculations were supported by institutional funds provided to JSM from the Voiland School of Chemical Engineering and Bioengineering. The authors also thank Zhehao Wei from WSU for some of the TPR experimental effort and Dr. Renqin Zhang from WSU for his efforts with the DFT calculations.

Appendix A. Supplementary material

Supplementary data associated with this article can be found, in the online version, at <http://dx.doi.org/10.1016/j.jcat.2013.05.020>.

References

- [1] G.W. Huber, S. Iborra, A. Corma, *Chem. Rev.* 106 (2006) 4044–4098.
- [2] D.C. Elliott, E.G. Baker, D. Beckman, Y. Solantausta, V. Tolénhiemo, S.B. Gevert, C. Hornell, A. Ostman, B. Kjellström, *Biomass* 22 (1990) 251–269.
- [3] J.C. Serrano-Ruiz, J.A. Dumesic, *Energy Environ. Sci.* 4 (2011) 83–99.
- [4] P.R. Patwardhan, P.A. Johnston, R.C. Brown, B.H. Shanks, in: *American Chemical Society*, 2010, pp. PETR-39.
- [5] P.R. Patwardhan, R.C. Brown, B.H. Shanks, *ChemSusChem* 4 (2011) 1629–1636.
- [6] M.A. Gonzalez-Borja, D.E. Resasco, *Energy Fuel* 25 (2011) 4155–4162.
- [7] I. Graca, J.M. Lopes, M.F. Ribeiro, F.R. Ribeiro, H.S. Cerqueira, M.B.B. de Almeida, *Appl. Catal. B-Environ.* 101 (2011) 613–621.
- [8] J.B.S. Bredenberg, M. Huuska, J. Rätty, M. Korpio, *J. Catal.* 77 (1982) 242–247.
- [9] A. Centeno, E. Laurent, B. Delmon, *J. Catal.* 154 (1995) 288–298.
- [10] E. Laurent, B. Delmon, *Appl. Catal. A* 109 (1994) 77–96.
- [11] M. Ferrari, S. Bosmans, R. Maggi, B. Delmon, P. Grange, *Catal. Today* 65 (2001) 257–264.
- [12] V.N. Bui, D. Laurenti, P. Afanasiev, C. Geantet, *Appl. Catal. B* 101 (2011) 239–245.
- [13] J. Zakzeski, P.C.A. Bruijninx, A.L. Jongerius, B.M. Weckhuysen, *Chem. Rev.* 110 (2010) 3552–3599.
- [14] E. Laurent, B. Delmon, *J. Catal.* 146 (1994) 281–291.
- [15] H.Y. Zhao, D. Li, P. Bui, S.T. Oyama, *Appl. Catal. A-General* 391 (2011) 305–310.
- [16] J. Wildschut, F.H. Mahfud, R.H. Venderbosch, H.J. Heeres, *Ind. Eng. Chem. Res.* 48 (2009) 10324–10334.
- [17] X.L. Zhu, L.L. Lobban, R.G. Mallinson, D.E. Resasco, *J. Catal.* 281 (2011) 21–29.
- [18] R. Runnebaum, T. Nimmanwudipong, D. Block, B. Gates, *Catal. Lett.* 141 (2010) 1–4.
- [19] T. Nimmanwudipong, R. Runnebaum, D. Block, B. Gates, *Catal. Lett.* 141 (2011) 1–5.
- [20] D.C. Elliott, T.R. Hart, *Energy Fuels* 23 (2009) 631–637.
- [21] D.C. Elliott, *Energy Fuel* 21 (2007) 1792–1815.
- [22] F.D. Mercader, M.J. Groeneveld, S.R.A. Kersten, N.W.J. Way, C.J. Schaverien, J.A. Hogendoorn, *Appl. Catal. B-Environ.* 96 (2010) 57–66.
- [23] E. Furimsky, *Appl. Catal. A* 199 (2000) 147–190.
- [24] R.K. Sharma, N.N. Bakhshi, *Energy Fuel* 7 (1993) 306–314.
- [25] D.-Y. Hong, S.J. Miller, P.K. Agrawal, C.W. Jones, *Chem. Commun.* 46 (2010) 1038–1040.
- [26] J. Wildschut, I. Melian-Cabrera, H.J. Heeres, *Appl. Catal. B-Environ.* 99 (2010) 298–306.
- [27] J. Gagnon, S. Kaliaguine, *Ind. Eng. Chem. Res.* 27 (1988) 1783–1788.
- [28] V.M.L. Whiffen, K.J. Smith, *Energy Fuel* 24 (2010) 4728–4737.
- [29] Y. Romero, F. Richard, Y. Reneme, S. Brunet, *Appl. Catal. A-General* 353 (2009) 46–53.
- [30] N.B. Van, D. Laurenti, P. Afanasiev, C. Geantet, *Appl. Catal. B-Environ.* 101 (2011) 239–245.
- [31] F.D. Mercader, M.J. Groeneveld, S.R.A. Kersten, C. Geantet, G. Toussaint, N.W.J. Way, C.J. Schaverien, K.J.A. Hogendoorn, *Energy Environ. Sci.* 4 (2011) 985–997.
- [32] C.A. Fisk, T. Morgan, Y.Y. Ji, M. Crocker, C. Crofcheck, S.A. Lewis, *Appl. Catal. A-General* 358 (2009) 150–156.
- [33] C. Zhao, Y. Kou, A.A. Lemonidou, X.B. Li, J.A. Lercher, *Angew. Chem.-Int. Edit.* 48 (2009) 3987–3990.
- [34] A. Gutierrez, R.K. Kaila, M.L. Honkela, R. Slioor, A.O.I. Krause, *Catal. Today* 147 (2009) 239–246.
- [35] T. Prasomsri, A.T. To, S. Crossley, W.E. Alvarez, D.E. Resasco, *Appl. Catal. B-Environ.* 106 (2011) 204–211.
- [36] A.V. Bridgwater, *Catal. Today* 29 (1996) 285–295.

- [37] T.R. Carlson, Y.T. Cheng, J. Jae, G.W. Huber, *Energy Environ. Sci.* 4 (2011) 145–161.
- [38] R. French, S. Czernik, *Fuel Process. Technol.* 91 (2010) 25–32.
- [39] U.V. Mentzel, M.S. Holm, *Appl. Catal. A-General* 396 (2011) 59–67.
- [40] E. Putun, B.B. Uzun, A.E. Putun, *Energ Fuel* 23 (2009) 2248–2258.
- [41] Q. Lu, X.F. Zhu, W.Z. Li, Y. Zhang, D.Y. Chen, *Chin. Sci. Bull.* 54 (2009) 1941–1948.
- [42] T. Nimmanwudipong, R.C. Runnebaum, D.E. Block, B.C. Gates, *Energ Fuel* 25 (2011) 3417–3427.
- [43] Q. Lu, Z. Tang, Y. Zhang, X.F. Zhu, *Ind. Eng. Chem. Res.* 49 (2010) 2573–2580.
- [44] A. Aho, N. Kumar, A.V. Lashkul, K. Eranen, M. Ziolek, P. Decyk, T. Salmi, B. Holmbom, M. Hupa, D.Y. Murzin, *Fuel* 89 (2010) 1992–2000.
- [45] A.J. Foster, P.T.M. Do, R.F. Lobo, *Top. Catal.* 55 (2012) 118–128.
- [46] R.N. Olcese, M. Bettahar, D. Petitjean, B. Malaman, F. Giovanella, A. Dufour, *Appl. Catal. B* 115–116 (2012) 63–73.
- [47] A.M. Karim, C. Howard, B. Roberts, L. Kovarik, L. Zhang, D.L. King, Y. Wang, *ACS Catal.* 2 (2012) 2387–2394.
- [48] B. Ravel, M. Newville, *J. Synchrot. Radiat.* 12 (2005) 537–541.
- [49] M. Newville, *J. Synchrot. Radiat.* 8 (2001) 96–100.
- [50] S.I. Zabinsky, J.J. Rehr, A. Ankudinov, R.C. Albers, M.J. Eller, *Phys. Rev. B* 52 (1995) 2995–3009.
- [51] J.M. Sun, K.K. Zhu, F. Gao, C.M. Wang, J. Liu, C.H.F. Peden, Y. Wang, *J. Am. Chem. Soc.* 133 (2011) 11096–11099.
- [52] G. Kresse, J. Hafner, *Phys. Rev. B* 47 (1993) 558–561.
- [53] G. Kresse, J. Furthmuller, *Phys. Rev. B* 54 (1996) 11169–11186.
- [54] G. Kresse, D. Joubert, *Phys. Rev. B* 59 (1999) 1758–1775.
- [55] J.P. Perdew, Y. Wang, *Phys. Rev. B* 45 (1992) 13244–13249.
- [56] I. Makkonen, P. Salo, M. Alatalo, T.S. Rahman, *Phys. Rev. B* 67 (2003) 165415.
- [57] D.F. Johnson, D.E. Jiang, E.A. Carter, *Surf. Sci.* 601 (2007) 699–705.
- [58] G. Makov, M.C. Payne, *Phys. Rev. B* 51 (1995) 4014–4022.
- [59] N.K. Nag, *J. Phys. Chem. B* 105 (2001) 5945–5949.
- [60] F. Pinna, M. Signoretto, G. Strukul, S. Polizzi, N. Pernicone, *React. Kinet. Catal. Lett.* 60 (1997) 9–13.
- [61] Y.-H. Chin, R. Dagle, J. Hu, A.C. Dohnalkova, Y. Wang, *Catal. Today* 77 (2002) 79–88.
- [62] M.W. Tew, J.T. Miller, J.A. van Bokhoven, *J. Phys. Chem. C* 113 (2009) 15140–15147.
- [63] A.V. Ruban, H.L. Skriver, J.K. Norskov, *Phys. Rev. B* 59 (1999) 15990–16000.
- [64] A.U. Nilekar, A.V. Ruban, M. Mavrikakis, *Surf. Sci.* 603 (2009) 91–96.
- [65] C. Milone, G. Neri, A. Donato, M.G. Musolino, *J. Catal.* 159 (1996) 253–258.
- [66] Y.C. Lin, C.L. Li, H.P. Wan, H.T. Lee, C.F. Liu, *Energ Fuel* 25 (2011) 890–896.